# Radiative behavior of low-porosity ceramics: II–Experimental and numerical study of porous alumina up to high temperatures

Zi Kang Low, Alexey Novikov, Domingos de Sousa Meneses, Dominique Baillis

Version of Record: https://www.sciencedirect.com/science/article/pii/S0022407321003149
Manuscript_91601fd78c2644c1132cfd83d588149f

# Radiative behavior of low-porosity ceramics: II– Experimental and numerical study of porous alumina up to high temperatures

Z.K. Low[a,b,*], A. Novikov[b,c], D. De Sousa Meneses[c], D. Baillis[a]

[a] *Univ Lyon, INSA Lyon, CNRS, LaMCoS UMR5259, 69621 Villeurbanne, France.*
[b] *Saint-Gobain Research Provence, 84306 Cavaillon, France.*
[c] *CEMHTI, CNRS UPR3079, Univ. Orléans, 45071 Orléans, France.*

**Abstract**

We compare two methods of characterizing the radiative behavior of 22% porous sintered alumina disks containing μm-sized pores on the 1 μm to 7 μm wavelength range up to very high temperatures. The first consists of direct spectroscopic measurements of the normal-hemispherical reflectance and transmittance at room temperature, as well as the normal emittance up to 1300 °C. The second is a two-step multi-scale numerical approach: the volume radiative properties and surface reflectivity are first determined from physical optics computations on tomography-reconstructed microstructures, then applied to the resolution of the radiative transfer equation on an equivalent homogeneous medium to obtain the spectral reflectance, transmittance, and emittance. Uncertainties in the numerical results, mainly due to microstructural variability, are quantified through sensitivity studies. The good agreement between the experimental and numerical results confirm the ability of our proposed numerical approach to give accurate predictions of the high-temperature radiative behavior of porous ceramics.

*Keywords:* Porous ceramics, Radiative properties, Infrared spectroscopy, Radiative transfer equation (RTE), High temperature

## 1. Introduction

The knowledge of radiometric quantities such as the spectral reflectance, transmittance, or emittance of materials are of great interest notably for high-temperature applications [1–4], and a

*Corresponding author
*Email address:* zi.low@insa-lyon.fr (Z.K. Low)

## Nomenclature

First- and second-order tensors ("vectors" and "matrices") are written in **bold face**.

**Latin**

| | |
|---|---|
| $A$ | Area |
| $B$ | Blackbody radiance |
| $E$ | Emittance |
| $e$ | Basis vector |
| $f$ | Volume fraction |
| $h$ | Height |
| $I$ | Spectral radiance |
| $k$ | Absorption index |
| $\ell$ | Chord length |
| $m$ | Complex refractive index, $n + ik$ |
| $n$ | Real refractive index; Normal vector |
| $p$ | Parameter |
| $R$ | Reflectance |
| $S$ | Sensitivity |
| $T$ | Transmittance; Temperature |
| $u$ | Direction |
| $X$ | Input variable |
| $x$ | Position |
| $Y$ | Output/Observed variable |

**Greek**

| | |
|---|---|
| $\Delta$ | Difference; interval; absolute uncertainty |
| $\delta$ | Kronecker delta |
| $\phi$ | Scattering phase function |
| $\varphi$ | Azimuth angle |
| $\kappa$ | Absorption coefficient |
| $\lambda$ | Wavelength |
| $\mu$ | Direction cosine |
| $\rho$ | Reflectivity |
| $\sigma$ | Scattering coefficient |
| $\tau$ | Transmissivity |
| $\theta$ | Polar angle |
| $\Omega$ | Solid angle |

**Superscripts and Subscripts**

| | |
|---|---|
| $'$ | Modified quantity |
| $+, -$ | Positive/Negative neighbourhood |
| 0 | Reference; *in vacuo* |
| $*$ | Basic radiance |
| abs | Absorption |
| amb | Ambient |
| diff | Diffuse |
| eff | Effective |
| int | Internal |
| Fr | Fresnel |
| h | Hemispherical |
| inc | Incident |
| ext | External |
| m | Matrix |
| p | Pore/Particle |
| R | Related to reflection |
| sca | Scattering |
| spec | Specular |
| sub | Substrate |
| T | Related to transmission |
| tr | Transport |
| V | Per unit volume |

**Operators and accents**

| | |
|---|---|
| $\cdot$ | Dot product |
| $\langle\bullet\rangle$ | Weighted average |
| $\langle\!\langle\bullet\rangle\!\rangle$ | Stochastic mean |
| $\hat{\bullet}$ | Unit vector |

**Acronyms**

| | |
|---|---|
| DDA | Discrete dipole approximation |
| OH | Hydroxyl |
| RMS | Root-mean-squared |
| RTE | Radiative transfer equation |

wide array of experimental methods have been developed for their characterization [5–7]. In the case of semi-transparent materials such as metal oxide ceramics, these quantities depend not only on material composition, but also on extrinsic parameters such as sample thickness, surface roughness, and the morphology of pores and other heterogeneities [8–11]. To account for the influence of some of these parameters, inverse methods based on minimizing the differences between theoretical predictions and experimental radiometric measurements are often used to identify the intrinsic effective radiative properties [12–17]. Alternatively, numerical methods are increasingly used to predict the radiometric quantities of interest from tomography-reconstructed or digitally generated microstructures. These methods are more suitable for the study of microstructure-property relations compared to inverse methods, as a large number of microstructurally different samples may be characterized at a lower cost [8, 18].

In the so-called "discrete-scale" approach [19], the quantities of interest are determined by simulating the radiation-matter interaction at the microstructural level. Direct Monte Carlo ray-tracing on 3D microstructures, usually assuming locally smooth interfaces that reflect and refract specularly [8, 16, 20–23], is a popular choice when heterogeneities are large and far apart compared to the wavelength. When this is not the case, numerical resolution of Maxwell's equations should be performed [11, 24], though the high computational cost limits its application to very small geometries. On the other hand, a less computationally demanding "continuum-scale" approach treats the heterogeneous material as an equivalent homogeneous medium [10, 17], and solves for the radiometric quantities of interest using the radiative transfer equation (RTE) while usually assuming smooth boundaries [3]. Accurate microstructure-based determination of the effective radiative properties is the challenge in this case: most past work relied on analytical microstructure-property relations [4], ray-tracing simulations [25–27], or the independent scattering hypothesis coupled with Mie theory or electromagnetic scattering computations [10, 28].

This paper, which is the second of two papers on the infrared radiative behavior of low-porosity ceramics, presents two methods of characterizing the radiometric properties of thin samples of a 22% porous alumina ceramic with μm-sized pores up to very high temperatures. Infrared spectroscopy measurements of the room-temperature normal-hemispherical reflectance and transmittance as well as the normal emittance up to 1300 °C are first performed. These are then compared

to numerical simulations of the same radiometric quantities at the same temperatures, obtained through a two-step multi-scale approach. The first step, described in detail in our first paper [29], consists of performing physical optics computations on 3D tomography-reconstructed microstructures to determine the effective radiative properties of the porous alumina ceramic. This novel approach, developed for ceramics with a weakly absorbing solid matrix and requiring only knowledge of the (temperature-dependent) complex refractive indexes of the different phases present, takes into account wave effects and dependent scattering by heterogeneities close in size to the wavelengths of interest. Our first paper concluded with analytical relations linking the porosity to the volume radiative properties and non-specular surface reflectivity of the porous alumina. These effective radiative properties are then applied to the second modeling step described in this paper, in which the reflectance, transmittance, and emittance are simulated via an RTE-based "continuum-scale" approach that considers non-specular boundaries of the equivalent homogeneous medium. Our present experimental and numerical studies aim to provide insights into the microstructural phenomena governing the high-temperature radiative behavior, and to validate the proposed multi-scale numerical method (notably the physical optics approach used to determine the effective radiative properties).

Section 2 describes the samples used in this study, and the experimental methods used for microstructural and radiometric characterization. Section 3 briefly summarizes the numerical method and key results of our first paper [29], then presents the RTE-based model used to predict the reflectance, transmittance, and emittance of the samples. Section 4 then presents and compares the experimental and numerical results, with the uncertainties in numerical results quantified through a sensitivity study.

## 2. Experimental procedure

### *2.1. Material and microstructure*

The studied material is a high-purity porous alumina ceramic, fabricated as plane-parallel disk samples for the infrared spectroscopy measurements (presented in section 2.2). A raw powder mix composed of 99% $\alpha$-alumina by mass, with a volume median grain diameter of 2.9 μm, was

first dispersed in water to form a homogeneous slurry, then air-dried and ground back up into powder form. Uniaxial pressing at 10 MPa in a cylindrical mold followed by sintering at 1650 °C for 6 hours gave porous sintered alumina cylinders 33 mm in diameter. Finally, plane-parallel cuts perpendicular to the cylinder axis were made with a precision saw to obtain disks of thickness $h = 2.0 \pm 0.1$ mm. The machined samples were heat-treated at 800 °C for 6 hours to remove all organic pollutants.

Scanning electron microscopy (Hitachi TM3030, 15 kV accelerating voltage, backscattered electrons mode) was performed at Saint-Gobain Research Provence (Cavaillon, France) on polished samples of the porous alumina ceramic (see Figure 1). The Fiji software [30] was then used to perform binarization, denoising, and microstructural analysis on the micrographs. Note that in our companion paper [29] we also presented the X-ray tomography and image processing protocol used to obtain the 3D microstructure.

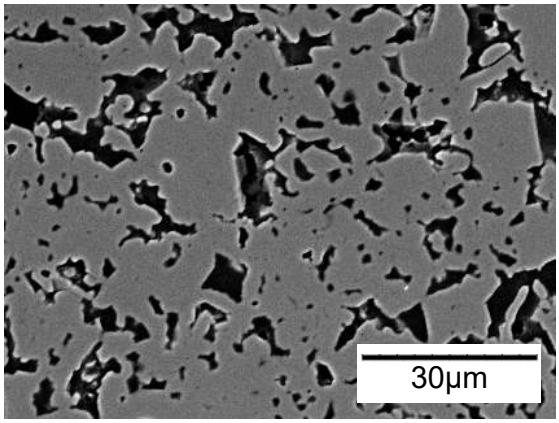


Figure 1: Scanning electron micrograph of a polished section of the porous alumina ceramic, with pores in black.

Physical measurements were also performed at Saint-Gobain Research Provence (Cavaillon, France) on the porous ceramic cylinders:

- A total porosity of $f_p = 0.22 \pm 0.02$ was measured on the cylinders by dividing their apparent density (caliper method) by the known density of the alumina powder mix. Open porosity measurements via the water immersion and saturation method [31] gave almost identical results, showing that little to no closed porosity is negligible (note that the porosity was also estimated through void pixel counting on 15 electron micrographs giving $f_p = 0.20 \pm 0.07$,

which is in good agreement with the physical measurement). We thus consider $f_\mathrm{p} = 0.22 \pm 0.02$ as the nominal porosity for the remainder of this study.

- We also performed pore size measurements just to check that the different methods and samples agree: the mean pore chord length [32] is estimated at $\langle\langle \ell_\mathrm{p} \rangle\rangle = 1.8 \pm 0.3\,\mu\mathrm{m}$ from the electron micrographs (which is in good agreement with value found on the tomographic reconstruction [29]). It agrees with the value of $\langle\langle \ell_\mathrm{p} \rangle\rangle \approx 4f_\mathrm{p}/A_\mathrm{V} = 1.2 \pm 0.2\,\mu\mathrm{m}$ measured using mercury intrusion porosimetry ($A_\mathrm{V}$ is the specific surface area) [33, 34]. The difference between the physical measurement and the image processing result may be attributed to the hypothesis of cylindrical pores in mercury intrusion porosimetry, which leads to underestimation when throats are present [34].

### *2.2. Infrared spectroscopy*

The spectral radiometric quantities of interest (reflectance, transmittance, and/or emittance) are measured on the 2 mm thick disks of diameter 33 mm, for vacuum wavelengths $\lambda_0$ between 1 µm and 10 µm from room temperature up to 1300 °C using two setups developed at the CEMHTI laboratory (Orléans, France), briefly described here.

At room temperature, the normal-hemispherical reflectance $R_\mathrm{h}$ and transmittance $T_\mathrm{h}$ are acquired using a 6-inch integrating sphere with infragold coating and a liquid-nitrogen-cooled mercury cadmium telluride detector, both coupled to a Fourier transform infrared spectrometer (Bruker Vertex 70) purged with dry air [6]. Measurements were performed at least 4 times (both sides of two samples) and averaged to account for the influence of material variability, which incidentally is quite low in the present case. Other sources of uncertainty include imperfections in the integrating sphere [35] and background parasite fluxes [6]. Taking all these sources into account, the absolute uncertainty is estimated to lie between 0.01 and 0.02 in the general case. However, in the present case where transmission is low, the uncertainty in $T_\mathrm{h}$ is estimated at 0.005 as some sources of uncertainty (e.g., those due the integrating sphere coating and opening) scale with magnitude of the measured signal. According to Kirchhoff's law [2], the room-temperature normal emittance

$E$, equal to the absorbance, is then calculated from $R_h$ and $T_h$ as follows:

$$E = 1 - R_h - T_h \tag{1}$$

At high temperatures, the normal emittance $E$ of a sample maintained at a constant elevated temperature $T$ is directly measured as the ratio of the spectral intensity emitted by the sample to that emitted by a blackbody at the same temperature [5]. The apparatus, shown in Figure 2 and described in detail in reference [7], consists of a reference blackbody furnace and a sample heating system mounted on a computer-controlled turntable within a purged enclosure. Two Fourier transform spectrometers (Bruker Vertex 80v working under vacuum, and Bruker Vertex 70 purged with dry air) enable measurements from the far infrared to the visible range. The flux emitted by the sample in the normal direction within an aperture of diameter 1 mm is measured and compared to the reference blackbody flux, with supplementary measurements to quantify and correct for the parasite fluxes from the instruments. To minimize the axial temperature gradient within the sample, a 500 W $CO_2$ laser (Coherent K500) separated equally by a beam splitter is used to heat the sample on both faces. The temperature of the sample is determined by using the spectrometer as a pyrometer at the known Christiansen wavelength of alumina ($\approx 10\,\mu m$) where it exhibits blackbody-like emissivity [36]. This methods allows the direct measurement of $E$ with an absolute uncertainty of 0.02 at extreme temperatures up to 2500 K.

Interested readers are invited to consult references [6] and [7] for more details on the apparatus used in this study.

## 3. Numerical method

The normal-hemispherical reflectance $R_h$ and transmittance $T_h$ of the porous alumina samples are simulated using a multi-scale approach presented in this section, then used to calculate the normal emittance $E$ via equation (1). In this approach, effective volume and surface radiative properties of the porous alumina material are first calculated using analytical relations, deduced from microstructure-based-simulation results of a novel physical optics model proposed in our companion paper [29]. We calculated effective radiative properties at selected temperatures from

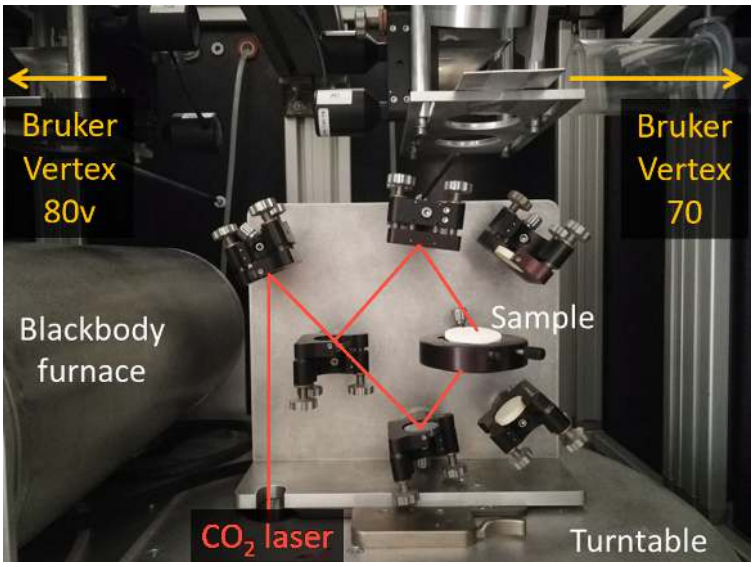


Figure 2: Apparatus at the CEMHTI laboratory (Orléans, France) used to measure the high-temperature emittance [7].

room temperature up to 1300 °C, which covers common service temperatures for refractory alumina. These effective properties are then used to model the reflectance and transmittance of the porous alumina disks under normal collimated illumination, by resolving the radiative transfer equation (RTE) on an equivalent homogeneous medium.

### *3.1. Effective radiative properties modeling with a physical optics based approach*

The effective radiative properties modeling approach proposed in our companion paper [29] has been developed for porous or multiphase materials with a homogeneous weakly absorbing dominant phase (henceforth referred to as the matrix, denoted with subscript $m$) having a much higher volume fraction compared to the other phases (pore or particle heterogeneities, denoted with subscript $p$). As the porous alumina samples in the present study contains 78% of high-purity $\alpha$-alumina by volume, with grain sizes exceeding one-tenth of the wavelengths of interest allowing grain boundary effects to be neglected [37], they fit the description. The model computes scattering and absorption in tomography-reconstructed volume elements of the material using the discrete dipole approximation (DDA) [38, 39], which takes into account physical optics effects and dependent scattering when heterogeneities are small and close to each other compared to the wavelength.

We determined the effective radiative properties of the porous alumina at temperatures $T$ =

22 °C, 800 °C, 1000 °C, and 1300 °C for selected wavelengths between $\lambda_0 = 1\,\mu m$ and $\lambda_0 = 7\,\mu m$. For each investigated temperature, we provided the spectral complex refractive index $n_m + ik_m$ of the sintered alumina matrix as input, obtained through directional averaging [40] of the birefringent complex refractive indexes of $\alpha$-alumina monocrystals [36]. Values are given in Table 1:

| $\lambda_0$ | $T = 22\,°C$ | | $T = 800\,°C$ | | $T = 1000\,°C$ | | $T = 1300\,°C$ | |
|---|---|---|---|---|---|---|---|---|
| (μm) | $n_m$ | $k_m$ | $n_m$ | $k_m$ | $n_m$ | $k_m$ | $n_m$ | $k_m$ |
| 1.0 | 1.718 | $1.36 \times 10^{-41}$ | 1.665 | $4.17 \times 10^{-7}$ | 1.645 | $6.88 \times 10^{-7}$ | 1.629 | $5.84 \times 10^{-7}$ |
| 1.5 | 1.712 | $8.12 \times 10^{-21}$ | 1.659 | $5.93 \times 10^{-7}$ | 1.640 | $9.86 \times 10^{-7}$ | 1.624 | $8.38 \times 10^{-7}$ |
| 2.0 | 1.704 | $7.22 \times 10^{-14}$ | 1.651 | $7.36 \times 10^{-7}$ | 1.632 | $1.24 \times 10^{-6}$ | 1.617 | $1.05 \times 10^{-6}$ |
| 3.0 | 1.680 | $4.25 \times 10^{-9}$ | 1.628 | $9.31 \times 10^{-7}$ | 1.611 | $1.61 \times 10^{-6}$ | 1.595 | $1.40 \times 10^{-6}$ |
| 4.0 | 1.644 | $3.43 \times 10^{-7}$ | 1.594 | $6.66 \times 10^{-6}$ | 1.578 | $1.20 \times 10^{-5}$ | 1.564 | $1.84 \times 10^{-5}$ |
| 5.0 | 1.594 | $2.78 \times 10^{-5}$ | 1.547 | $1.42 \times 10^{-4}$ | 1.534 | $2.02 \times 10^{-4}$ | 1.521 | $2.77 \times 10^{-4}$ |
| 6.0 | 1.527 | $2.37 \times 10^{-4}$ | 1.482 | $9.97 \times 10^{-4}$ | 1.473 | $1.34 \times 10^{-3}$ | 1.462 | $1.74 \times 10^{-3}$ |
| 7.0 | 1.435 | $1.94 \times 10^{-3}$ | 1.390 | $6.03 \times 10^{-3}$ | 1.392 | $6.91 \times 10^{-3}$ | 1.385 | $7.06 \times 10^{-3}$ |

Table 1: Complex refractive index of sintered alumina at the studied temperatures.

DDA computations were performed on a large number of subvolumes of the reconstructed material (8 to 125 depending on wavelength and volume element size). This allowed us to extract analytical porosity-property relations for porosities ranging from a few percent up to $f_p \approx 0.3$, and also to quantify the uncertainty in the computed effective radiative properties as the root-mean-squared (RMS) deviation between DDA results on all subvolumes and the analytical relation. Key conclusions from our companion paper [29] are summarized below:

- DDA simulations confirmed that thanks to the low alumina absorptivity on the absorption coefficient $\kappa_{eff}$ may be calculated to 7% uncertainty on the wavelength range of interest with the analytical relation proposed by Dombrovsky et al. [41] for porous ceramics with a weakly absorbing solid phase:

$$\kappa_{eff} = \frac{4\pi k_m}{\lambda_0} f_m \tag{2}$$

  Indeed, as pure alumina monocrystal data is used as input for the solid matrix, $k_m$ very low for the considered temperatures and wavelengths ($\leq 6 \times 10^{-3}$) and $\kappa_{eff}$ scales linearly with the matrix fraction $f_m$. The values of $\kappa_{eff}$ at the nominal porosity $f_p = 0.22 = 1 - f_m$ of the porous alumina samples are plotted for the studied wavelengths and temperatures in

Figure 3a. Note that as a logarithmic scale is used, the ±7% error bars are barely visible. At room temperature, the extremely low $\kappa_{\text{eff}}$ (less than 1 $\text{m}^{-1}$) for wavelengths between 1 µm to 4 µm are not represented to improve legibility (practically no absorption occurs in the mm-sized samples at this temperature and wavelength range).

- Based on our discussion in the companion paper [29], we found that the porous alumina material, initially with scattering coefficient $\sigma_{\text{eff}}$ and anisotropic phase function $\phi_{\text{eff}}$, is appropriately modeled with a transport scattering coefficient $\sigma_{\text{tr}}$ associated with an isotropic phase function $\phi_{\text{tr}} = (4\pi)^{-1}$ instead [42]:

$$\sigma_{\text{tr}} = \sigma_{\text{eff}}(1 - g_{\text{sca}}) = \sigma_{\text{eff}}\left(1 - \int_{4\pi} \phi_{\text{eff}}(\hat{\boldsymbol{u}}, \hat{\boldsymbol{u}}')\left|\hat{\boldsymbol{u}} \cdot \hat{\boldsymbol{u}}'\right| \mathrm{d}\Omega'\right) \tag{3}$$

where $\hat{\boldsymbol{u}}$ and $\hat{\boldsymbol{u}}'$ are the unit direction vectors of the incident and scattered light respectively, $\mathrm{d}\Omega'$ is the elementary solid angle associated with $\hat{\boldsymbol{u}}'$, and $4\pi$ is the solid angle of a sphere which represents the entire angular space. Note that in this work $\phi_{\text{eff}}$ is normalized such that $\int_{4\pi} \phi_{\text{eff}}(\hat{\boldsymbol{u}}, \hat{\boldsymbol{u}}')\, \mathrm{d}\Omega' = 1$.

The values of $\sigma_{\text{tr}}$ simulated using the DDA were well described with a second-order polynomial function of the porosity:

$$\sigma_{\text{tr}} = p_1 f_{\text{p}} + p_2 f_{\text{p}}^2 \tag{4}$$

with coefficients $p_1(\lambda_0, T)$ and $p_2(\lambda_0, T)$ identified from DDA results for every temperature and wavelength. The values of $\sigma_{\text{tr}}$ predicted with these correlations at the nominal porosity of $f_{\text{p}} = 0.22$ are plotted in Figure 3b. Error bars indicate the uncertainty of ±20.8%, estimated by taking the RMS deviation between all DDA results and the analytical relation, and reflects the high microstructural variability.

- For the surface reflectivity, we assume that the surface of the studied porous alumina is smooth everywhere save where pores are present. DDA numerical results in our companion paper [29] for the case of normal illumination by light of wavelength $\lambda = \lambda_0 = 2\,\mu\text{m}$

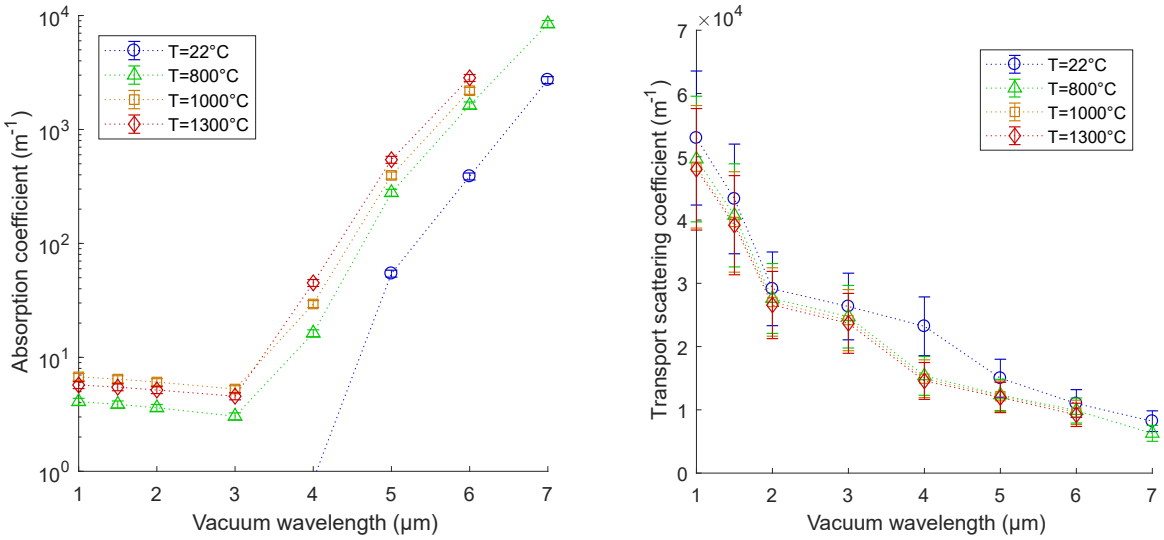


(a) Absorption coefficient.

(b) Transport scattering coefficient.

Figure 3: Spectral volume radiative properties of the porous alumina ceramic, evaluated at its nominal porosity $f_\mathrm{p} = 0.22$, for four different temperatures $T$.

were rather well described by a geometrical-optics-based analytical model that simply considers perfectly diffuse reflection for incident radiation incident on the pore phase, and perfectly specular reflection according to Fresnel's equations for the remaining radiation. The directional-hemispherical reflectivity $\rho_\mathrm{h}$ and transmissivity $\tau_\mathrm{h}$ for incidence direction $\hat{\boldsymbol{u}}$ are then modeled as follows [29]:

$$\rho_\mathrm{h}(\hat{\boldsymbol{u}}) = \underbrace{f_\mathrm{m}\rho_\mathrm{Fr}(\hat{\boldsymbol{u}})}_{\rho_\mathrm{spec}(\hat{\boldsymbol{u}})} + \underbrace{f_\mathrm{p}\,\langle\rho_\mathrm{Fr}\rangle}_{\rho_\mathrm{diff}} \tag{5a}$$

$$\tau_\mathrm{h}(\hat{\boldsymbol{u}}) = \underbrace{f_\mathrm{m}(1-\rho_\mathrm{Fr}(\hat{\boldsymbol{u}}))}_{\tau_\mathrm{spec}(\hat{\boldsymbol{u}})} + \underbrace{f_\mathrm{p}(1-\langle\rho_\mathrm{Fr}\rangle)}_{\tau_\mathrm{diff}} \tag{5b}$$

$\rho_\mathrm{Fr}(\hat{\boldsymbol{u}})$ is the specular reflectivity given by Fresnel's equations [1], here computed for light in vacuum incident on an alumina surface of refractive index $n_\mathrm{m}$. $\langle\rho_\mathrm{Fr}\rangle$ is the diffuse reflectivity obtained by the following weighted average of $\rho_\mathrm{Fr}$ [42, 43]:

$$\langle\rho_\mathrm{Fr}\rangle \equiv \int_{\hat{\boldsymbol{u}}'\cdot\hat{\boldsymbol{n}}<0} 2\rho_\mathrm{Fr}(\hat{\boldsymbol{u}}')\left|\hat{\boldsymbol{u}}'\cdot\hat{\boldsymbol{n}}\right| \mathrm{d}\Omega' \tag{6}$$

where $\hat{\boldsymbol{n}}$ is the normal vector pointing outwards from the surface. For normally incident

light on a surface with $n_m = 1.718$ (corresponding to the sintered alumina phase at room temperature and $\lambda_0 = 1\,\mu m$), equation (5a) gives $\rho_h = 0.0814$. Uncertainties are estimated at 22.6% on $\rho_h$ and 27% on $\rho_{spec}$, mainly due to neglected wave effects and microstructural variability.

These analytical relations are then used to determine the effective volume and surface radiative properties of the porous alumina ceramic studied in this paper, by setting $f_p = 0.22$.

In the next section, the determined effective radiative properties are applied to the simulation of radiometric measurements on the 2 mm thick disks from room temperature to 1300 °C. While the uncertainties in some of the effective radiative properties are rather high, sensitivity studies presented in section 4.2 show that they have limited influence on the simulated radiometric properties.

### *3.2. Reflectance, transmittance, and emittance modeling*

For all the considered temperatures, we first simulate the normal-reflectance $R_h$ and transmittance $T_h$ of the porous alumina disks by resolving the radiative transfer equation (RTE) on an equivalent homogeneous medium. With these two quantities, the normal emittance $E$ is then calculated via Kirchhoff's law (equation (1)). The RTE-based model, which has the particularity of considering non-specular reflection and refraction at boundaries, is described here.

We consider a semi-infinite plane-parallel slab of thickness $h$ placed in vacuum ($n_{amb} = 1$), illuminated on one face by a collimated beam at incidence angle $\theta_{inc}$ (= 0 in the present work). The slab, at uniform temperature $T$, is composed of a homogeneous absorbing-scattering material prescribed the absorption ($\kappa_{eff}$) and transport scattering ($\sigma_{tr}$) in Figure 3. Per classic assumptions [14, 28, 44] of 1D radiative transfer, azimuthal symmetry, and negligible self-emission, the RTE simplifies to [2]:

$$\mu \frac{\partial I^*(x,\mu)}{\partial x} = -(\sigma_{tr} + \kappa_{eff}) I^*(x,\mu) + \frac{\sigma_{tr}}{4\pi} \int_{4\pi} I^*(x,\mu')\, d\Omega' \tag{7}$$

where $x$ is the position along the thickness direction $\hat{\boldsymbol{e}}_x$, and $\mu \equiv \hat{\boldsymbol{u}} \cdot \hat{\boldsymbol{e}}_x$ is the direction cosine for the unit direction vector $\hat{\boldsymbol{u}}$ associated with the solid angle $d\Omega$. Note we solve for the spectral basic

radiance $I^*$ to account for the conservation of étendue [45] when light refracts at the boundary between the surrounding vacuum medium and the slab:

$$I^* = \frac{I}{n^2} \tag{8}$$

where $I$ is the spectral radiance (radiance per unit vacuum wavelength) and $n$ is the local refractive index: $n = 1$ in the surrounding vacuum (hence $I^* = I$ for $x < 0$ or $x > h$) and $n > 1$ within the slab (hence $I^* \neq I$ for $0 < x < h$).

As the slab is under normal collimated illumination, the incident radiance $I^*_{\text{inc}}$ is only non-zero at $x = 0^-$, within a narrow solid angle $\Delta\Omega$ about the normal direction $\mu = 1$.

In section 3.1, we chose to model the directional-hemispherical reflectivity $\rho_h$ of the slab boundary under external illumination from the surrounding vacuum medium as the sum of a perfectly specular component $\rho_{\text{spec}}$ and a perfectly diffuse component $\rho_{\text{diff}}$ (equation (5a)). These terms are henceforth denoted with the superscript "ext" to distinguish them from their counterparts for radiation arriving at the boundary from within the material (internal illumination), denoted with the superscript "int". Based on microscopic reversibility principles [46], we assume that $\rho^{\text{int}}$ is also modeled in the same manner as $\rho^{\text{ext}}$ using equations (5a) and (6), with $\rho^{\text{int}}_{\text{Fr}} = 1$ for incident angles exceeding the critical angle for total internal reflection.

The boundary conditions are then expressed using the definitions in equations (5a) and (5b),

- For $x = 0^+$:

$$\begin{aligned} I^*(\mu > 0) = \tau^{\text{ext}}_{\text{spec}}(\mu) I^*_{\text{inc}} \delta_{1-\mu} + \frac{\tau^{\text{ext}}_{\text{diff}}}{\pi} \int_{\Delta\Omega} I^*_{\text{inc}} \, \mathrm{d}\Omega' \\ + \rho^{\text{int}}_{\text{spec}}(\mu'_{\text{R}}) I^*(\mu'_{\text{R}}) + \frac{\rho^{\text{int}}_{\text{diff}}}{\pi} \int_{\mu'<0} I^*(\mu') \mu' \, \mathrm{d}\Omega' \end{aligned} \tag{9a}$$

  where $\delta$ represents the Kronecker delta, here defined as $\delta_X = 1$ if $X = 0$, and $\delta_X = 0$ otherwise;

- For $x = h^-$:

$$I^*(\mu < 0) = \rho^{\text{int}}_{\text{spec}}(\mu'_{\text{R}}) I^*(\mu'_{\text{R}}) + \frac{\rho^{\text{int}}_{\text{diff}}}{\pi} \int_{\mu'>0} I^*(\mu') \mu' \, \mathrm{d}\Omega' \tag{9b}$$

where $\mu'_{\mathrm{R}} = -\mu$ represents the direction prior to a specular reflection event that reflected light towards the direction $\mu$. These boundary conditions are illustrated in Figure 4.

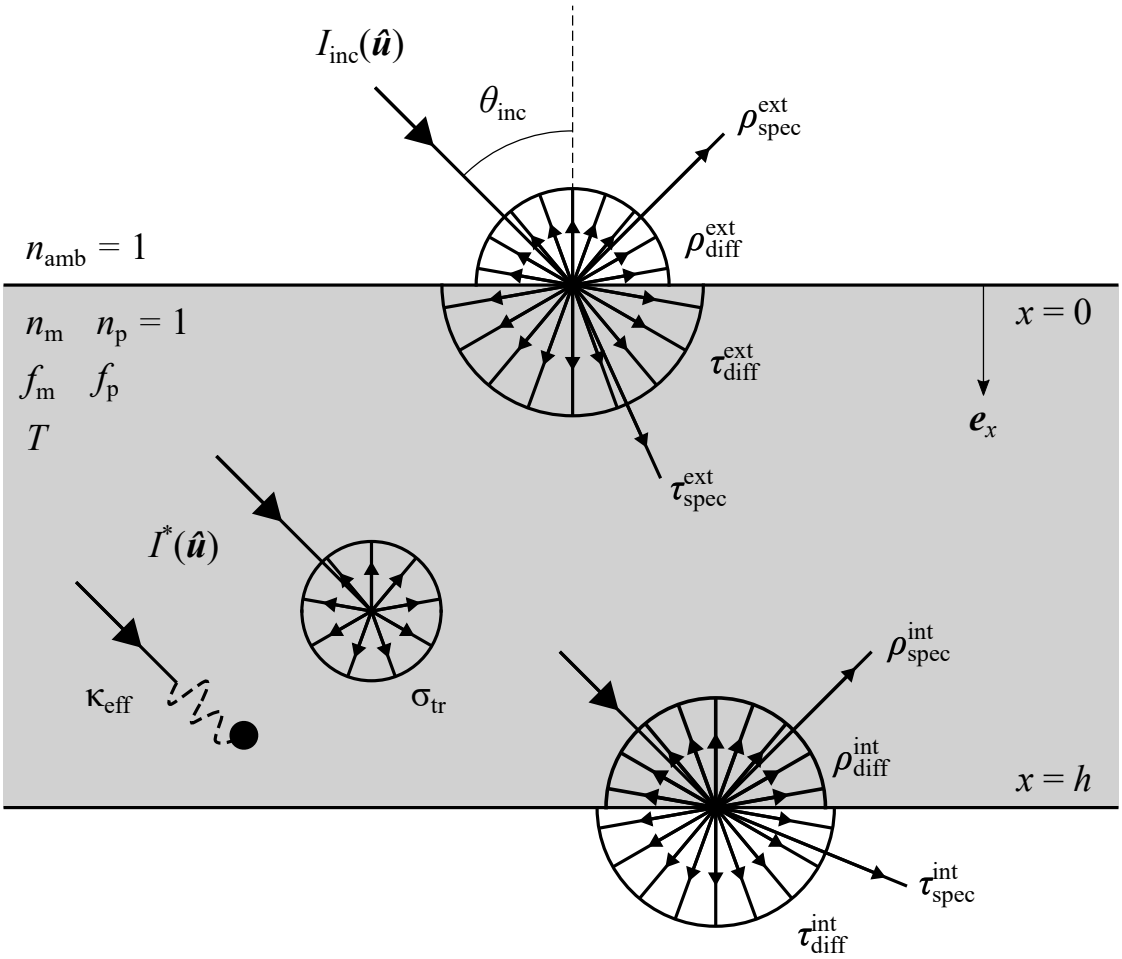


Figure 4: Diagram of the reflectance and transmittance model.

Equations (7) and (9) were resolved with the Monte Carlo method [2, 23]: converged results were obtained using $10^6$ equal-energy packets. The reflected and transmitted radiance fields are

then calculated:

$$I^*(x=0^-,\mu<0) = \rho^{\text{ext}}_{\text{spec}}(\mu) I^*_{\text{inc}} \delta_{1+\mu} + \frac{\rho^{\text{ext}}_{\text{diff}}}{\pi} \int_{\Delta\Omega} I^*_{\text{inc}} \, \mathrm{d}\Omega' + \tau^{\text{int}}_{\text{spec}}(\mu'_{\text{T}}) I^*(x=0^+,\mu'_{\text{T}}) + \frac{\tau^{\text{int}}_{\text{diff}}}{\pi} \int_{\mu'<0} I^*(x=0^+,\mu')\mu' \, \mathrm{d}\Omega' \tag{10a}$$

$$I^*(x=h^+,\mu>0) = \tau^{\text{int}}_{\text{spec}}(\mu'_{\text{T}}) I^*(x=h^-,\mu'_{\text{T}}) + \frac{\tau^{\text{int}}_{\text{diff}}}{\pi} \int_{\mu'>0} I^*(x=h^-,\mu')\mu' \, \mathrm{d}\Omega' \tag{10b}$$

where $\mu'_{\text{T}}$ represents the direction prior to an outgoing specular refraction event that refracted light towards the direction $\mu$, calculated using the Snell-Descartes law [45]: $n^2_{\text{m}}(1-{\mu'_{\text{T}}}^2) = n^2_{\text{amb}}(1-\mu^2)$.

The normal-hemispherical reflectance $R_{\text{h}}$ and transmittance $T_{\text{h}}$ are then obtained as follows:

$$R_{\text{h}} = \frac{\int_{\mu<0} I^*(x=0^-,\mu)\mu \, \mathrm{d}\Omega}{\int_{\Delta\Omega} I^*_{\text{inc}} \, \mathrm{d}\Omega'} \tag{11a}$$

$$T_{\text{h}} = \frac{\int_{\mu>0} I^*(x=h^+,\mu)\mu \, \mathrm{d}\Omega}{\int_{\Delta\Omega} I^*_{\text{inc}} \, \mathrm{d}\Omega'} \tag{11b}$$

after which the normal emittance is simply calculated as $E = 1 - R_{\text{h}} - T_{\text{h}}$ per equation (1).

## 4. Results and Discussion

### *4.1. Comparison of experimental and numerical results*

Figure 5 compares the experimentally measured reflectance ($R_{\text{h}}$) and transmittance ($T_{\text{h}}$) at room temperature to the ones simulated at selected wavelengths using our new physical-optics-based approach. An excellent agreement is found between the two results at wavelengths smaller than 2.5 µm and greater than 5 µm, well within experimental uncertainties (±0.01), which is extremely encouraging for validation of our proposed numerical approach.

Note that the error bars represent numerical uncertainties denoted $\Delta Y$ for an observed quantity $Y \in \{R_{\text{h}}, T_{\text{h}}, E\}$, evaluated assuming that the input parameters $X$ vary independently of one another:

$$(\Delta Y)^2 = \sum_X \left( S_Y(X) \frac{\Delta X}{X_0} \times 100\% \right)^2 \tag{12}$$

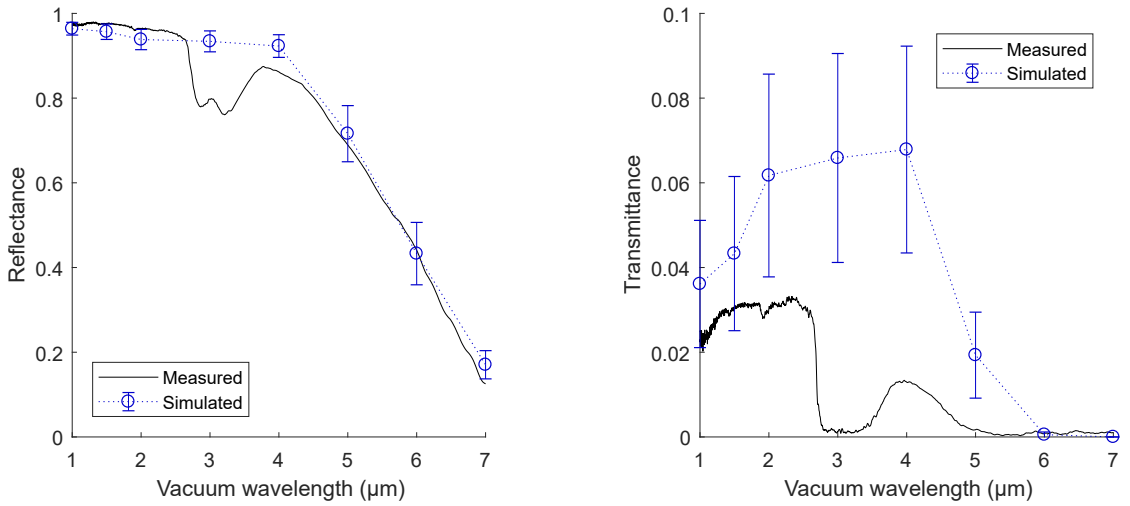


(a) Normal-hemispherical reflectance.

(b) Normal-hemispherical transmittance.

Figure 5: Measured (lines) and simulated (∘) spectral normal-hemispherical reflectance and transmittance of the porous alumina disks at room temperature ($T$ = 22 °C).

where $(\Delta X/X_0)\times 100\%$ is the relative uncertainty in % on $X$, and $S_Y(X)$ is the sensitivity coefficient defined as the variation in $Y$ per % increase in $X$, all other input parameters being constant:

$$S_Y(X) = \left.\frac{\partial Y}{\partial X}\right|_{X_0} \frac{X_0}{100\%} \tag{13}$$

Note that $S_Y(X)$ is studied later in section 4.2, with values given in Figure 7. Table 2 summarizes the input parameters $X$ considered and their relative uncertainties. The computed uncertainties range from 0.01 to 0.07 depending on the radiometric quantity and wavelength.

| $\frac{\Delta\kappa_{\text{eff}}}{\kappa_{\text{eff},0}}$ | $\frac{\Delta\sigma_{\text{tr}}}{\sigma_{tr,0}}$ | $\frac{\Delta\rho^{\text{ext}}_{\text{spec}}}{\rho^{\text{ext}}_{\text{spec},0}} = \frac{\Delta\rho^{\text{int}}_{\text{spec}}}{\rho^{\text{int}}_{\text{spec},0}}$ | $\frac{\Delta\rho^{\text{ext}}_{\text{diff}}}{\rho^{\text{ext}}_{\text{diff},0}} = \frac{\Delta\rho^{\text{int}}_{\text{diff}}}{\rho^{\text{int}}_{\text{diff},0}}$ | $\frac{\Delta h}{h_0}$ |
|---|---|---|---|---|
| 7% | 21% | 26% | 40% | 5% |

Table 2: Uncertainties in input parameters: effective absorption coefficient ($\kappa_{\text{eff}}$), transport scattering coefficient ($\sigma_{\text{tr}}$), specular ($\rho_{\text{spec}}$) and diffuse ($\rho_{\text{diff}}$) components of the surface reflectivity (for both external/internal illumination), and sample thickness ($h$).

Between 2.5 µm and 5 µm, a sharp dip is observed in the measured spectra for both $R_{\text{h}}$ and $T_{\text{h}}$ but is absent from the numerical results. This difference between numerical and experimental results at room temperature is expected: it is due to the characteristic absorption by hydroxyl (OH) groups and adsorbed water molecules, which are almost always present on the surface of alumina

ceramics [47] but are not taken into account in the input data for our numerical model. Recall that we worked with complex refractive indexes derived from measurements on impurity-free alumina monocrystals [36]. Precise determination of impurity content and its influence on radiometric quantities is generally challenging: Rozenbaum et al. [8] recently proposed an inverse method to identify the OH content in porous silica, which combines emittance measurements on dense and porous samples with discrete-scale ray-tracing simulations.

While this absorption peak is clearly seen on the room-temperature emittance curve in Figure 6, it is absent from the high-temperature emittance spectra since near-complete desorption of the OH groups occur at 800 °C and above [47]. With the increase in temperature, the absorption front (sharp increase in emittance between $\lambda_0 \approx 3\,\mu\text{m}$ and $\lambda_0 \approx 7\,\mu\text{m}$) shifts slightly towards shorter wavelengths under the influence of multiphonon processes [36]. The low emittance at wavelengths below 2.5 µm for all temperatures is a testament to the high purity of the alumina matrix.

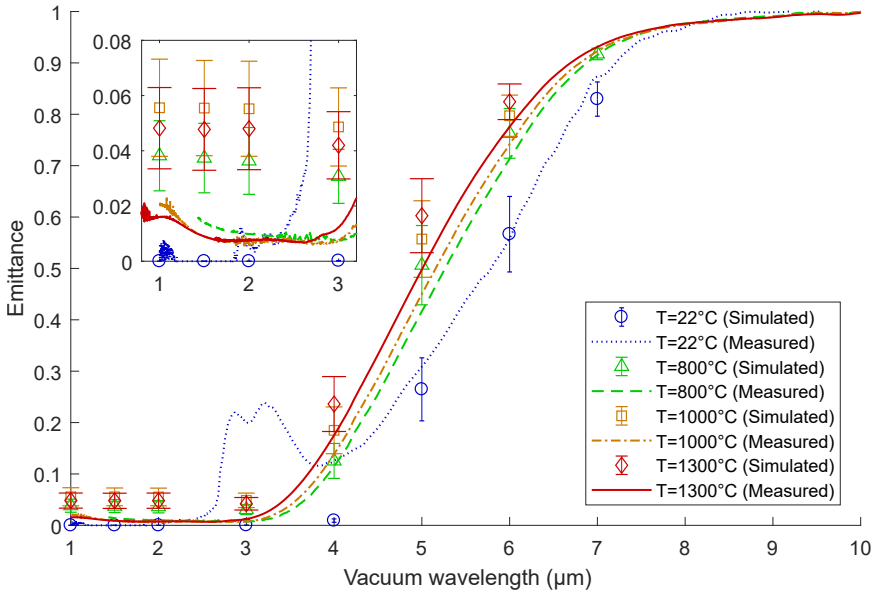


Figure 6: Measured (lines) and simulated (symols) spectral normal emittance of the porous alumina disks at different temperatures $T$: 22 °C (dotted lines vs. ○), 800 °C (dashed lines vs. △), 1000 °C (dash-dotted lines vs. □), 1300 °C (continuous lines vs. ⋄). The inset shows the near-zero emittances at wavelengths between 1 µm and 3 µm.

In the absence of OH absorption peaks, the high-temperature emittance spectra are extremely well reproduced by the numerical models. The numerical results appear to slightly overestimate the experimental results at all wavelengths, though the differences still remain within their re-

spective confidence intervals. Notably, uncertainties in the temperature and reference blackbody flux determination during high-temperature emittance measurements give an estimated absolute uncertainty of ±0.02.

These results validate our numerical modeling approach, notably the DDA-based method proposed in our companion paper [29] to compute the effective radiative properties, the use of alumina monocrystal data as input while neglecting grain boundary scattering.

### *4.2. Sensitivity study*

Figure 7 shows the sensitivity coefficients $S_Y(X)$ defined in equation (13) as a function of wavelength $X = \left\{\sigma_{\mathrm{tr}}, \kappa_{\mathrm{eff}}, \rho_{\mathrm{spec}}, \rho_{\mathrm{diff}}, h\right\}$ and $Y = \{R_{\mathrm{h}}, T_{\mathrm{h}}, E\}$ at temperature $T = 800\,^{\circ}\mathrm{C}$ (note that similar trends are also observed at the other studied temperatures). The magnitude of $S_Y(X)$ indicates the sensitivity of $Y$ to small changes in $X$, while its sign indicates whether a small increase in $X$ leads to an increase ($S_Y > 0$) or decrease ($S_Y < 0$) in $Y$.

We observe that while $S_Y$ is generally quite low, it is always non-zero except when the observed quantity $Y$ is null or very low. The non-zero value of $S_h$ shows the extrinsic nature of the radiometric quantities. Some interesting observations are summarized below:

- The signs of $S_Y(\sigma_{\mathrm{tr}})$ and $S_Y(\kappa_{\mathrm{eff}})$ are physically coherent: increasing $\sigma_{\mathrm{tr}}$ increases $R_{\mathrm{h}}$, decreases $T_{\mathrm{h}}$ and decreases $E$, while increasing $\kappa_{\mathrm{eff}}$ decreases $R_{\mathrm{h}}$, decreases $T_{\mathrm{h}}$ and increases $E$. The similar trends in their magnitudes suggest that the influence of $\sigma_{\mathrm{tr}}$ and $\kappa_{\mathrm{eff}}$ are correlated. This is discussed further in section 4.3.

- The sensitivity coefficients for $\rho_{\mathrm{spec}}$ and $\rho_{\mathrm{diff}}$ are very similar, since $R_{\mathrm{h}}$, $T_{\mathrm{h}}$ and $E$ are quite insensitive to the exact angular distribution of radiative energy. Surprisingly, an increase in either of these parameters decrease $R_{\mathrm{h}}$ while increasing $T_{\mathrm{h}}$ and $E$. This is because a large part of the total reflected radiation is actually composed of radiation initially transmitted into the slab before exiting it from the illuminated face. When $\rho_{\mathrm{spec}}$ or $\rho_{\mathrm{diff}}$ is increased, the fraction of incident radiation transmitted into the slab decreases, and the probability of internal radiation exiting the slab also decreases. This "trapping" effect by the slab boundaries [23] increases the emittance especially, and also the transmittance to a smaller extent.

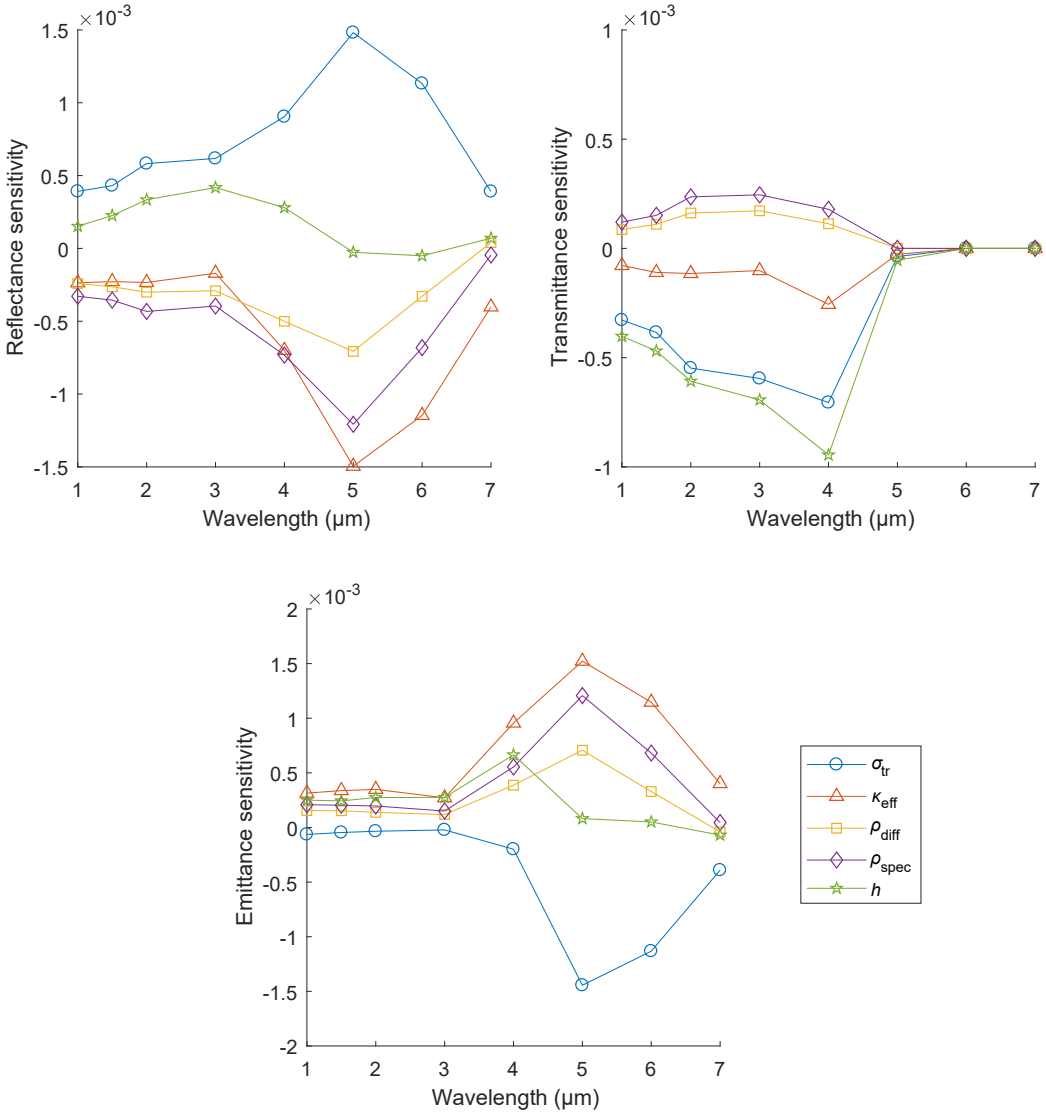


Figure 7: Spectral sensitivity coefficients (see equation (13)) for the normal-hemispherical reflectance (left), normal-hemispherical transmittance (center) and normal emittance (right) at 800 °C, with respect to five input parameters: transport scattering coefficient $\sigma_{tr}$ ($\circ$), absorption coefficient $\kappa_{eff}$ ($\triangle$), diffuse reflectivity component $\rho_{diff}$ ($\square$), specular reflectivity component $\rho_{spec}$ ($\diamond$), and slab thickness $h$ ($\star$).

- While the thickness $h$ is the most influential parameter on $T_h$ on the semi-transparent range ($\lambda_0 < 5\,\mu m$), its effect on $R_h$ and $E$ on this range appears limited. Indeed, when scattering dominates, the optical paths traveled by radiation within the material is generally tortuous with multiple internal reflections off the boundary, and are therefore insensitive to small changes in $h$. In the opaque range ($\lambda_0 \geq 5\,\mu m$), $h$ has practically no influence on all radiometric properties since radiation-matter interaction is limited to a small region close to the incident surface.

### *4.3. Influence of porosity*

Before concluding, we study the influence of porosity on the radiometric properties by comparing the room-temperature reflectance ($R_h$), transmittance ($T_h$) and emittance ($E$) of our 22% porous alumina disks to those of a dense sintered alumina. Literature data on dense sintered alumina are often obtained from experiments on fine-grained samples in which grain boundary scattering due to material birefringence, impurities, and residual pores is significant [17, 37, 48]. This makes it difficult to draw meaningful conclusions as to the role of porosity in the present material, in which grain boundary scattering is shown to be negligible by our experimental and numerical results. We therefore considered a hypothetical dense sample with no volume scattering, modeled with Fresnel's equations using the same complex refractive index $n_m + ik_m$ used for the DDA computations (section 3.1. Figure 8 shows a remarkable increase in $R_h$ by more than 0.8 (and a corresponding decrease in $T_h$) due to the porosity of 22%. While the increase in reflectance and decrease in transmittance are natural when pores are present, the magnitude of these variations is much higher than past investigations on porous ceramics [8, 21]. This shows the interest in being able to incorporate physical optics effects in radiative transfer modeling.

In addition, between the wavelengths of 4 µm to 8 µm on the emittance (=absorbance) plot, we see that the absorption front is significantly modified by the presence of pores, with higher emittance in the porous material between 4 µm to 6 µm and higher emittance in the dense material beyond 6 µm. In fact, when the porosity increases, two competing mechanisms are in play: on one hand, the increased volume scattering within the porous material prolongs the optical paths traveled by light and thus the probability of being absorbed [21]; on the other hand, the probability

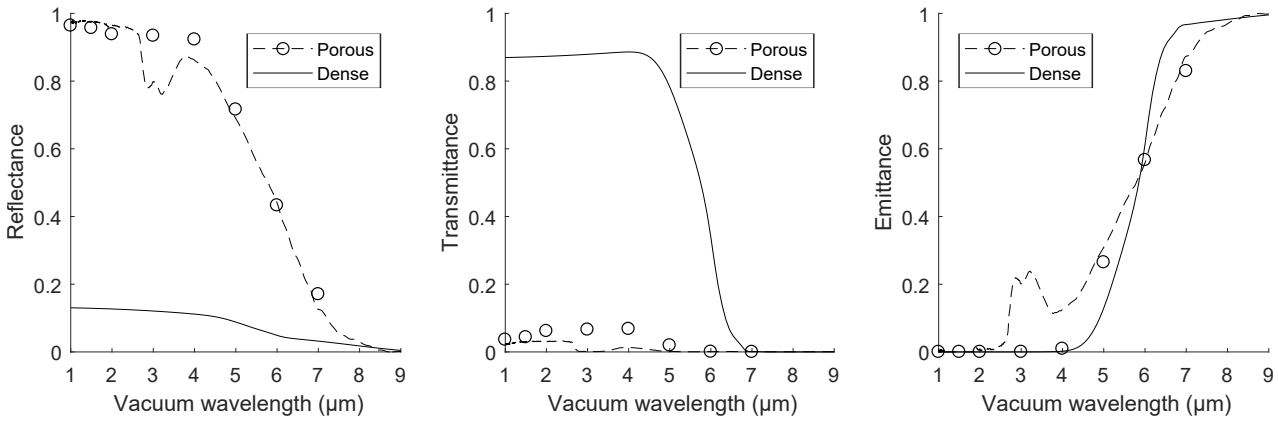


Figure 8: Room-temperature normal-hemispherical reflectance (left), normal-hemispherical transmittance (center), and normal emittance (right): measurements and physical-optics-based simulations on porous alumina disks (dashed lines and ∘ respectively) compared to calculations with Fresnel's equations for a hypothetical dense alumina (continuous lines).

of being absorbed for the same optical path length is lower in the porous material than in the dense material due to the lower matrix fraction. The prevalence of one over another depends on the relative magnitudes of the absorbing and scattering coefficients and also on the shape of the phase function, which explains the correlation observed between the sensitivity coefficients taken with respect to $\sigma_{tr}$ and $\kappa_{eff}$ (see section 4.2). In the present case, it would appear that the first mechanism dominates for wavelengths below 6 μm, while for wavelengths beyond this threshold the second mechanism dominates.

## 5. Conclusion

The reflectance, transmittance and emittance of porous alumina disks are measured from room temperature up to 1300 °C are compared to numerical results obtained using a novel multi-scale approach: effective radiative properties are first determined from physical optics computations on 3D microstructures, then applied to the simulation of an equivalent homogeneous medium using the radiative transfer equation (RTE).

A sensitivity study using the RTE-based model was performed to quantify the uncertainties in numerical results, mainly arising from microstructural variability due to the small volume elements used in physical optics modeling. Uncertainties in the simulated radiometric quantities (reflectance, transmittance and emittance) are generally low, varying from 0.01 to 0.07 depending

on wavelength. The sensitivity coefficients also provided insight to the influence of different input parameters and the physical phenomena in play.

The excellent agreement between experimental and numerical results confirm the validity of the proposed multi-scale approach, in particular the microstructure-based modeling approach proposed in our companion paper [29] to determine the effective radiative properties. The extremely high reflectance and low transmittance in the present porous alumina samples for such a low porosity is never observed in the geometrical optics limit. It illustrates the strong influence of small heterogeneities on the macro-scale radiative properties, and highlights the need for more accurate physical-optics-based radiative transfer models.

Future work should focus on using the DDA numerical results to establish more accurate analytical modeling of microstructure-property relations, taking into account not just the porosity as we did, but also other parameters such pore size or pore shape. Application of the present DDA-RTE approach to the simulation and validation on other types of materials (e.g., multiple particle phases), or other types of radiometric quantities (e.g., bidirectional quantities) would also be of great interest to test the capabilities of the proposed approach.

## 6. Acknowledgments

This research was supported by Saint-Gobain Research (SGR) Provence and the French National Association for Research and Technology (ANRT) through the CIFRE grant number 2017/0775. The authors would like to express their gratitude to L. San Miguel (SGR Provence), L. Pierrot (SGR Provence) and J. Meulemans (SGR Paris) for their insight and discussions that greatly improved the research; to Y. Millot (SGR Provence) for sample preparation and physical microstructural characterization; to J. Adrien (MATEIS) and N. Naouar (LaMCoS) for assistance with X-ray tomography; and last but not least, to R. Coquard (EC2 Modélisation) and S. Cunsolo (ex-LaMCoS) for helpful discussions on radiative transfer modeling.

## References

[1] Q. Brewster, Thermal Radiative Transfer and Properties, John Wiley & Sons, Inc., 1992.

[2] J. Howell, M. Menguc, R. Siegel, Thermal Radiation Heat Transfer, 6th Edition, 6 ed., Taylor & Francis, 2015.

[3] L. A. Dombrovsky, J. H. Randrianalisoa, W. Lipiński, D. Baillis, Approximate analytical solution to normal emittance of semi-transparent layer of an absorbing, scattering, and refracting medium, Journal of Quantitative Spectroscopy and Radiative Transfer 112 (2011) 1987–1994.

[4] Y. Li, H. W. Chen, X. L. Xia, G. Y. Ma, H. P. Tan, Prediction of high-temperature radiative properties of copper, nickel, zirconia, and alumina foams, International Journal of Heat and Mass Transfer 148 (2020) 119154.

[5] J. M. Palmer, The measurement of transmission, absorption, emission and reflection, in: M. Bass (Ed.), Handbook of Optics, Optical Society of America, Volume II, 2 ed., McGraw-Hill, 1994, pp. 25.1–25.25.

[6] A. Dupleix, D. De Sousa Meneses, M. Hughes, R. Marchal, Mid-infrared absorption properties of green wood, Wood Science and Technology 47 (2013) 1231–1241.

[7] D. De Sousa Meneses, P. Melin, L. Del Campo, L. Cosson, P. Echegut, Apparatus for measuring the emittance of materials from far infrared to visible wavelengths in extreme conditions of temperature, Infrared Physics and Technology 69 (2015) 96–101.

[8] O. Rozenbaum, C. Blanchard, D. De Sousa Meneses, Determination of high-temperature radiative properties of porous silica by combined image analysis, infrared spectroscopy and numerical simulation, International Journal of Thermal Sciences 137 (2019) 552–559.

[9] R. Coquard, D. Baillis, D. Quenard, Energy & Buildings Numerical and experimental study of the IR opacification of polystyrene foams for thermal insulation enhancement, Energy & Buildings 183 (2019) 54–63.

[10] X. Dai, S. Haussener, Optical characterization of multi-scale morphologically complex heterogeneous media – application to snow with soot impurities, Journal of Quantitative Spectroscopy and Radiative Transfer 206 (2018) 378 – 391.

[11] X. Chen, C. Zhao, B. Wang, Microstructural effect on radiative scattering coefficient and asymmetry factor of anisotropic thermal barrier coatings, Journal of Quantitative Spectroscopy and Radiative Transfer 210 (2018) 116 – 126.

[12] R. Lopes, L. M. Moura, D. Baillis, J. F. Sacadura, Directional spectral emittance of a packed bed: Correlation between theoretical prediction and experimental data, Journal of Heat Transfer 123 (2001) 240–249.

[13] B. Zeghondy, E. Iacona, J. Taine, Experimental and RDFI calculated radiative properties of a mullite foam, International Journal of Heat and Mass Transfer 49 (2006) 3702–3707.

[14] L. A. Dombrovsky, H. K. Tagne, D. Baillis, L. Gremillard, Near-infrared radiative properties of porous zirconia ceramics, Infrared Physics & Technology 51 (2007) 44 – 53.

[15] L. Dombrovsky, D. Baillis, Thermal Radiation in Disperse Systems: An Engineering Approach, Begell House, 2010.

[16] B. Bouvry, L. Del Campo, D. De Sousa Meneses, O. Rozenbaum, R. Echegut, D. Lechevalier, M. Gaubil, P. Echegut, Hybrid Methodology for Retrieving Thermal Radiative Properties of Semi-Transparent Ceramics, Journal of Physical Chemistry C 120 (2016) 3267–3274.

[17] P. Yang, Q. Cheng, Z. Zhang, Radiative Properties of Ceramic Al2O3, AlN, and Si3N4—II: Modeling, International Journal of Thermophysics 38 (2017) 124.

[18] O. Rozenbaum, D. De Sousa Meneses, P. Echegut, Texture and porosity effects on the thermal radiative behavior of alumina ceramics, International Journal of Thermophysics 30 (2009) 580–590.

[19] J. Petrasch, S. Haussener, W. Lipiński, Discrete vs. continuum-scale simulation of radiative transfer in semitransparent two-phase media, Journal of Quantitative Spectroscopy and Radiative Transfer 112 (2011) 1450–1459.

[20] B. Singh, M. Kaviany, Independent theory versus direct simulation of radiation heat transfer in packed beds, International Journal of Heat and Mass Transfer 34 (1991) 2869 – 2882.

[21] B. Rousseau, J.-y. Y. Rolland, P. Echegut, L. Del Campo, D. De Sousa Meneses, P. Echegut, Modelling of the Thermal Radiative Properties of Oxide Ceramics, in: Proceedings of the 14th International Heat Transfer Conference, 13, 2010, pp. 1–6.

[22] J. Randrianalisoa, S. Haussener, D. Baillis, W. Lipiński, Radiative characterization of random fibrous media with long cylindrical fibers: Comparison of single- and multi-rte approaches, Journal of Quantitative Spectroscopy and Radiative Transfer 202 (2017) 220 – 232.

[23] S. Cunsolo, D. Baillis, N. Bianco, Improved Monte Carlo methods for computational modelling of thermal radiation applied to porous cellular materials, International Journal of Thermal Sciences 137 (2019) 161–179.

[24] B. Liu, X. Xia, X. Zhang, C. Sun, Spectral radiative properties of skeleton inner structure of ceramic foam based on ordered opal structure model, Journal of Quantitative Spectroscopy and Radiative Transfer 224 (2019) 279 – 288.

[25] R. Coquard, D. Baillis, Radiative characteristics of opaque spherical particles beds: A new method of prediction, Journal of Thermophysics and Heat Transfer 18 (2004) 178–186.

[26] W. Lipiński, J. Petrasch, S. Haussener, Application of the spatial averaging theorem to radiative heat transfer in two-phase media, Journal of Quantitative Spectroscopy and Radiative Transfer 111 (2010) 253–258.

[27] J. Randrianalisoa, D. Baillis, Radiative properties of densely packed spheres in semitransparent media: A new geometric optics approach, Journal of Quantitative Spectroscopy and Radiative Transfer 111 (2010) 1372 – 1388.

[28] S. Lallich, F. Enguehard, D. Baillis, Experimental Determination and Modeling of the Radiative Properties of Silica Nanoporous Matrices, Journal of Heat Transfer 131 (2009) 082701.

[29] Z. Low, D. Baillis, 1– a physical optics approach to predict the radiative properties of semi-transparent porous ceramics, 2020. In preparation.

[30] J. Schindelin, I. Arganda-Carreras, E. Frise, V. Kaynig, M. Longair, T. Pietzsch, S. Preibisch, C. Rueden, S. Saalfeld, B. Schmid, J.-Y. Tinevez, D. J. White, V. Hartenstein, K. Eliceiri, P. Tomancak, A. Cardona, Fiji: an open-source platform for biological-image analysis, Nature Methods 9 (2012) 676–682.

[31] U. Kuila, D. K. McCarty, A. Derkowski, T. B. Fischer, M. Prasad, Total porosity measurement in gas shales by

the water immersion porosimetry (wip) method, Fuel 117 (2014) 1115 – 1129.

[32] M. R. MacIver, M. Pawlik, Analysis of in situ microscopy images of flocculated sediment volumes, Chemical Engineering & Technology 40 (2017) 2305–2313.

[33] W. de Kruijf, J. Kloosterman, On the average chord length in reactor physics, Annals of Nuclear Energy 30 (2003) 549–553.

[34] P. A. Webb, An introduction to the physical characterization of materials by mercury intrusion porosimetry with emphasis on reduction and presentation of experimental data, Technical Report, Micromeritics Instrument Corp, Norcross, Georgia, 2001.

[35] B. Liu, Y. Yuan, Z. Y. Yu, X. Huang, H. P. Tan, Numerical investigation of measurement error of the integrating sphere based on the Monte-Carlo method, Infrared Physics and Technology 79 (2016) 121–127.

[36] J. F. Brun, L. del Campo, D. De Sousa Meneses, P. Echegut, Infrared optical properties of alpha-alumina with the approach to melting: gamma-like tetrahedral structure and small polaron conduction, Journal of Applied Physics 114 (2013) 223501.

[37] D. C. Harris, L. F. Johnson, L. Cambrea, L. Baldwin, M. Baronowski, E. Zelmon, W. B. Poston, J. D. Kunkel, M. Parish, M. R. Pascucci, J. J. Gannon, Jr, T.-c. Wen, Refractive index of infrared- transparent polycrystalline alumina, Optical Engineering 56 (2017) 077103.

[38] B. T. Draine, P. J. Flatau, Discrete-Dipole Approximation For Scattering Calculations, Journal of the Optical Society of America A 11 (1994) 1491.

[39] B. T. Draine, P. J. Flatau, Discrete-dipole approximation for periodic targets: theory and tests, Journal of the Optical Society of America A 25 (2008) 2693.

[40] L. A. Pajdzik, A. M. Glazer, Three-dimensional birefringence imaging with a microscope tilting-stage. I. Uniaxial crystals, Journal of Applied Crystallography 39 (2006) 326–337.

[41] L. Dombrovsky, J. Randrianalisoa, D. Baillis, L. Pilon, Use of Mie theory to analyze experimental data to identify infrared properties of fused quartz containing bubbles, Applied optics 44 (2005) 7021–7031.

[42] L. A. Dombrovsky, The use of transport approximation and diffusion-based models in radiative transfer calculations, Computational Thermal Sciences: An International Journal 4 (2012) 297–315.

[43] R. Siegel, C. Spuckler, Approximate solution methods for spectral radiative transfer in high refractive index layers, International Journal of Heat and Mass Transfer 37 (1994) 403 – 413.

[44] A. Kaemmerlen, C. Vo, F. Asllanaj, G. Jeandel, D. Baillis, Radiative properties of extruded polystyrene foams: Predictive model and experimental results, Journal of Quantitative Spectroscopy and Radiative Transfer 111 (2010) 865–877.

[45] J. Chaves, Introduction to Nonimaging Optics, 2 ed., CRC Press, 2017.

[46] B. H. Mahan, Microscopic reversibility and detailed balance. an analysis, Journal of Chemical Education 52 (1975) 299.

[47] Z. Łodziana, J. K. Nørskov, P. Stoltze, The stability of the hydroxylated (0001) surface of $\alpha$-Al2O3, Journal of Chemical Physics 118 (2003) 11179–11188.

[48] Q. Cheng, P. Yang, Z. Zhang, Radiative Properties of Ceramic Al2O3, AlN, and Si3N4: I. Experiments, International Journal of Thermophysics 37 (2016) 62.